

Magnetic Correlation Spectroscopy in CrSBr

Lukas Krelle, Ryan Tan, Daria Markina, Priyanka Mondal, Kseniia Mosina, Kevin Hagmann, Regine von Klitzing, Kenji Watanabe, Takashi Taniguchi, Zdenek Sofer, and Bernhard Urbaszek*



Cite This: *ACS Nano* 2025, 19, 33156–33163



Read Online

ACCESS |



Metrics & More



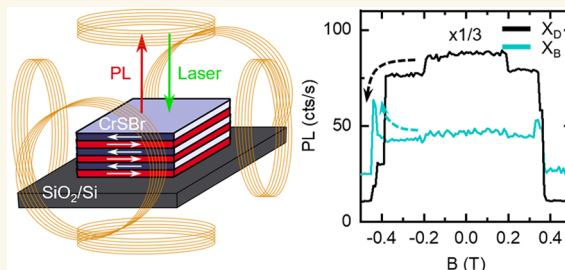
Article Recommendations



Supporting Information

ABSTRACT: CrSBr is an air-stable magnetic van der Waals semiconductor with strong magnetic anisotropy, where the interaction of excitons with the magnetic order enables the optical identification of different magnetic phases. Here, we study the magnetic anisotropy of multilayer CrSBr inside a three-axis vector magnet and correlate magnetic order and optical transitions in emission and absorption. We identify layer-by-layer switching of the magnetization through drastic changes in the optical emission and absorption energy and strength as a function of the applied magnetic field. We correlate optical transitions in reflection spectra with photoluminescence (PL) emission using transfer-matrix analysis and find that ferromagnetic and antiferromagnetic order between layers can coexist in the same crystal. In the multipeak PL emission, the intensity of energetically lower-lying transitions reduces monotonously with increasing field strength, whereas energetically higher-lying transitions around the bright exciton X_B brighten close to the saturation field. Using this contrasting behavior, we can therefore correlate transitions with each other.

KEYWORDS: CrSBr, magneto-optics, magnetic semiconductor, van der Waals materials, excitons, layered antiferromagnet



I. INTRODUCTION

Due to a plethora of tunable magnetic intra- and interlayer interactions,¹ layered magnetic materials have motivated research toward applications in data storage^{2,3} and spintronics.^{4,5} However, many-layered magnetic semiconductors like chromium trihalides and related materials suffer from instability under ambient conditions.^{6–9} Compared to these materials, the semiconducting layered antiferromagnet CrSBr exhibits a much higher stability in ambient conditions.^{10,11} It is well suited for fundamental studies of magnons,^{12–14} exciton–phonon coupling,^{15–17} and exciton–photon coupling^{18–22} as well as applications in magnetic devices exhibiting large negative magnetoresistance,^{23,24} tunable properties with magnetic fields,²⁵ and electrostatic doping,²⁶ as well as ion irradiation.^{27,28} CrSBr crystals are strongly anisotropic, which results in a strong dependence of the magnetic, optical, and electronic properties^{25,29,30} on the crystallographic axes.

The intricate interplay between excitons and the magnetic order in CrSBr enables the spectroscopic identification of different magnetic phases^{25,26,31} as well as spatial domains.²⁶ The spectroscopic signature of excitonic transitions is not limited to the topmost layer but also reveals information about deeper-lying layers,³² which is potentially an advantage compared to successful scanning probe techniques.^{33,34} Up to now, research has mainly focused on understanding the magnetic and excitonic properties of bulk systems and 1–4-layer systems. However, the study of multilayer systems, which

exhibit complex emission properties without the influence of strong exciton–photon coupling, has remained elusive.

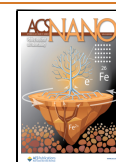
In this work, we study the anisotropic magnetic properties of CrSBr inside a vector magnet at low cryogenic temperatures. We use correlated spectral changes occurring with the application of a magnetic field to investigate the origin and connections of optical transitions present in multilayer samples of CrSBr. To this end, we fabricated two multilayer samples: one (14 layers; thickness determined by atomic force microscopy = 11.3 ± 0.2 nm) encapsulated in hexagonal boron nitride (hBN), and another one as-exfoliated (10 layers; thickness determined by atomic force microscopy = 8.2 ± 0.3 nm). We performed magnetic-field dependent photoluminescence (PL) and differential reflectance contrast (DR/R) measurements at $T = 4.7$ K and carefully tracked the emission energy and intensity to determine potential emission origins. Our measurements show that the ferromagnetic (FM) state is reached gradually throughout the crystal as different layers switch from the antiferromagnetic (AFM) to the FM order at different fields. We find phases close to the saturation field that show a superposition of spectral signatures of both the FM and AFM states.

Received: April 1, 2025

Revised: August 21, 2025

Accepted: August 21, 2025

Published: September 12, 2025



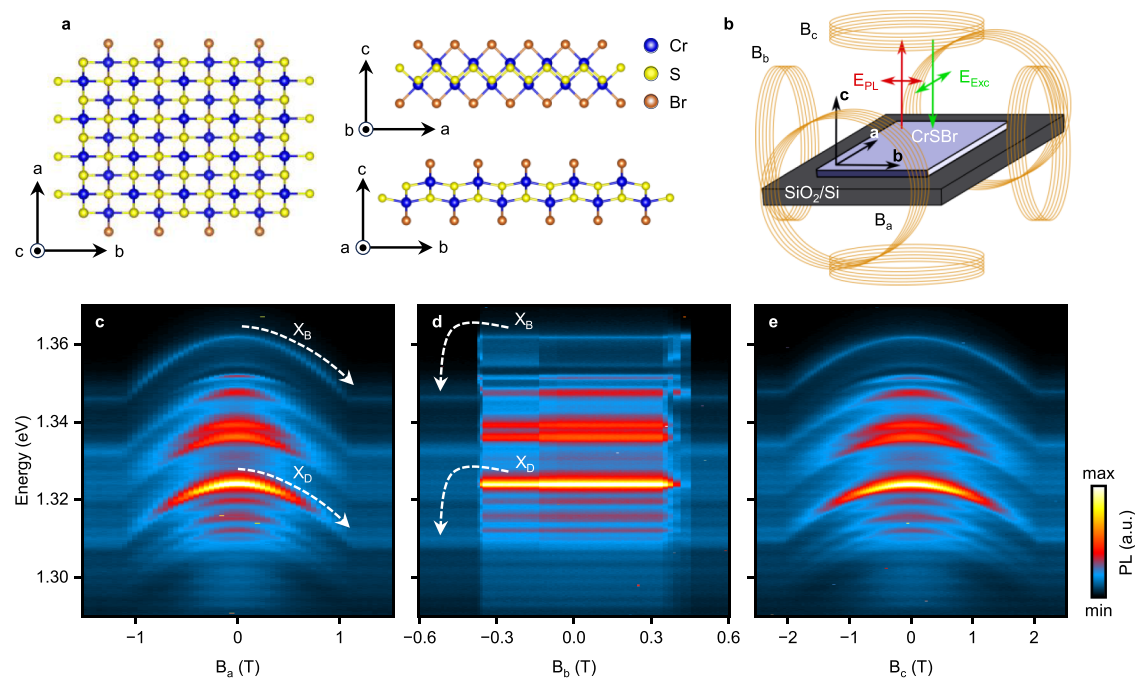


Figure 1. Experiments on CrSBr in a three-axis vector magnet. (a) CrSBr crystal structure. Crystallographic axes a , b , and c are indicated by arrows. (b) Sketch of a CrSBr sample inside the vector magnet and the orientation of laser and PL polarization with respect to crystallographic axes. (c–e) Exemplary PL magnetic field sweeps of the encapsulated sample for the same spatial spot along the crystal a , b , and c axes, respectively, displaying magnetic anisotropy, where $B_a \parallel a$, $B_b \parallel b$, and $B_c \parallel c$. Dashed white arrows are a guide for the eye for the evolution of X_D (at 1.324 eV at $B = 0$) and X_B (at 1.362 eV at $B = 0$) transitions.

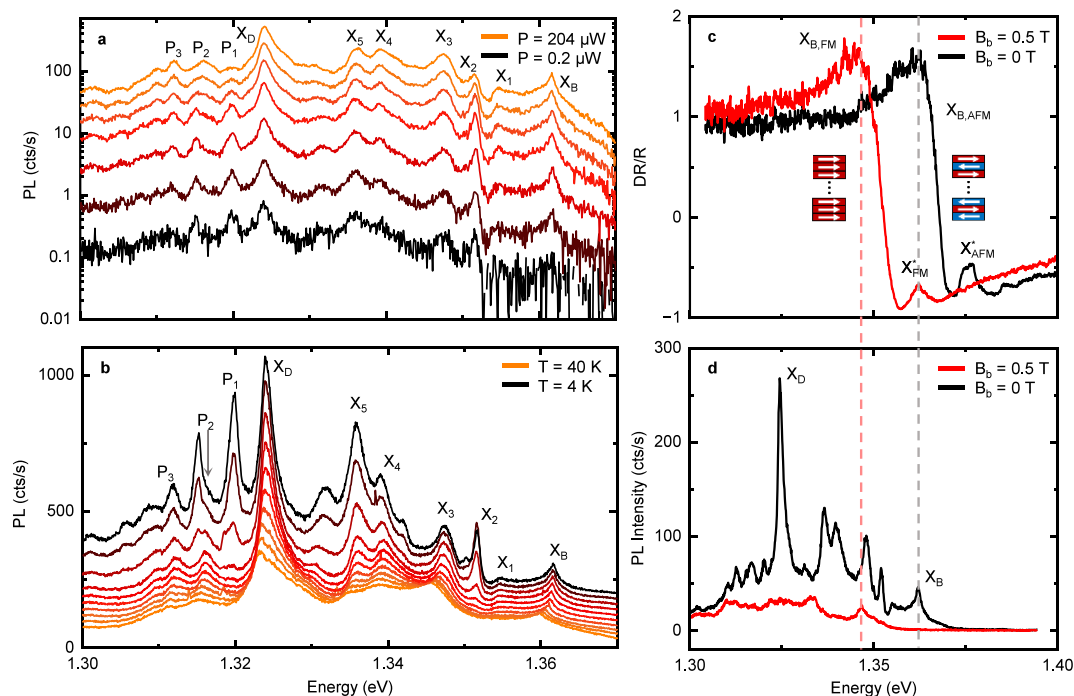


Figure 2. Influence of excitation power, temperature, and magnetic field on the optical properties of encapsulated 14-layer CrSBr. (a) Excitation power dependence of the PL emission at $B = 0$ T and $T = 4.7$ K. (b) Temperature dependence of the PL emission at $B = 0$ T and $10 \mu\text{W}$ excitation power. (c and d) DR/R and PL spectra of the 14-layer sample for the AFM (black) and FM (red) states. Emissions are as indicated in the main text. Dashed gray and red lines indicate the energy of X_B in the AFM and FM states, respectively.

Excitation-power-dependent and temperature-dependent PL measurements reveal several emission peaks that originate from trapped exciton species.

II. RESULTS AND DISCUSSION

As a first step in our detailed spectral analysis, we performed cryogenic magneto-optical spectroscopy inside a three-axis vector magnet, in which the crystallographic axes are aligned

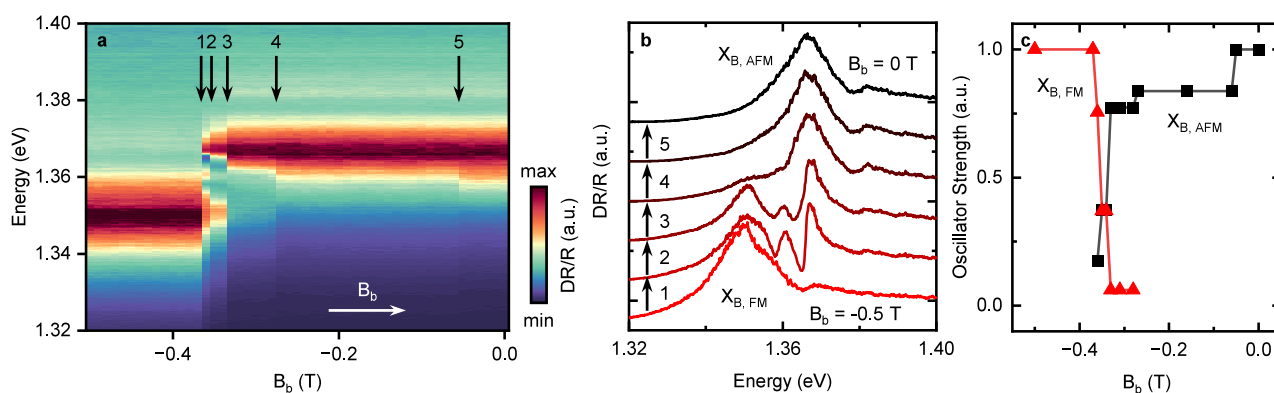


Figure 3. Layer-by-layer magnetization switching in 10-layer CrSBr. (a) False color plot of a DR/R measurement with magnetic field applied along the b axis. Arrows indicate the transition fields, and numbers indicate the transitions as in part b. (b) DR/R spectra of the six different layer magnetization configurations. (c) Normalized oscillator strengths of $X_{B,AFM}$ and $X_{B,FM}$ extracted from a Lorentzian oscillator model.

with the magnetic field axes as in earlier seminal work.²⁵ Parts a and b of Figure 1 display the crystal structure of CrSBr and the experimental configuration, respectively. Unless noted differently, we focus on the hBN-encapsulated 14-layer sample. We performed PL measurements at $T = 4.7$ K with an excitation energy of 1.959 eV, above the estimated band gap of CrSBr.^{25,29} First, we study the magnetic anisotropy of the material, which is clearly visible in the magnetic field sweeps along the crystal axes shown in Figure 1c,e for the same sample spot. At zero magnetic field, below the critical temperature, the layers show PL spectra associated with AFM order, as spins in adjacent layers point in the opposite direction along the crystal b axis.^{11,35,36} The application of a magnetic field rotates the magnetization such that beyond a certain saturation field all layers are magnetized along the same direction (i.e., parallel to the applied field) corresponding to FM order. We trace the change from AFM to FM order through changes in the PL energy.²⁵ The saturation fields along the different axes for the data shown are respectively $B_c^b = \pm 2.05 \pm 0.05$ T and $B_a^b = \pm 1.10 \pm 0.05$ T. Due to hysteresis effects, the saturation fields along b depend on the sweep direction with $B_b^b = +0.45 \pm 0.01$ and -0.37 ± 0.01 T. The continuous energy shift of the emission peaks for sweeps along the magnetic hard and intermediate axis allows the assignment of the emission peaks in the AFM and FM states, which we aim to identify. For comparison, the abrupt jumps at B_b^b make peak assignments between the optical emission in the AFM and FM states more challenging.

In our PL measurements, the linear excitation polarization is aligned with the crystal a axis, while the detection polarization is aligned with the b axis (Figure 1b). The crystal axes were determined via the maximum and minimum PL intensity for the b and a axes, respectively. Figure S1 displays the polarization dependence of the PL emission of encapsulated 14-layer CrSBr at $B = 0$ T. Due to the strong anisotropy of the material, the PL emission is highly linearly polarized, exhibiting maximum intensity along the b axis and about a factor of 200 weaker intensity along the a axis. Both samples show qualitatively similar PL spectra with a multitude of different emission peaks with narrow linewidths (on the order of millielectronvolts), as shown in Figure 2a,b,d for encapsulated 14-layer CrSBr and in Figure S2a,b,d for unencapsulated 10-layer CrSBr. Importantly, due to the small sample thickness, the rich spectra cannot stem from polaritonic states, as reported for bulk CrSBr layers,^{18,19} but from different excitonic species, their phonon replica and trapped states, which we aim to identify further.

In Figure 2d, we mark two transitions that will be of significance in our discussion: transition X_D , which is the strongest in PL, and transition X_B , which is visible in PL and is the strongest transition in terms of oscillator strength in DR/R (see below). Observing strong PL from transitions that have low oscillator strength resembles the rich PL spectra of WSe₂ monolayers with several exciton species.^{37–39} Apart from X_B and X_D , we find several emission peaks between X_B and X_D , which we label $X_{1–5}$, as well as three emissions below X_D , which we label $P_{1–3}$. In Table S1, we summarize the energies of the observed emission peaks for the AFM and FM order.

We performed excitation-power-dependent PL measurements, displayed in Figure 2a, to ensure that we capture all details of the complex spectra. Most of the emission peaks follow a linear power dependence, as displayed in Figure S3. We observe several emission peaks, of which we highlight X_2 and P_1 , that show signs of saturation at an excitation power of 50 μ W. Temperature-dependent measurements reveal that these emissions vanish very quickly around $T = 16$ K, as shown in Figure 2b. Additionally, these measurements reveal that the emission labeled P_2 is accompanied by another emission peak that dominates over P_2 at low temperatures and excitation powers. This emission peak also vanishes around $T = 16$ K. These observations are characteristic for excitons in shallow trapping potentials.^{40,41} As the temperature increases, the trapped excitons gain enough thermal energy to escape the trapping potential and the associated emission diminishes. Notably, of the multitude of emission peaks, only X_B , X_3 , and X_D remain present up to $T = 100$ K (see Figure S4 for measurements up to $T = 150$ K).

In the unencapsulated sample, the changes from low to high excitation power are more pronounced, as shown in Figure S2b. Here we focus on a low excitation power regime, in which both samples exhibit similar emission properties, as highlighted in the direct comparison in Figure S2a. We note that the emission peaks in the unencapsulated sample are blueshifted by 4 meV with respect to the encapsulated sample, most likely due to dielectric screening,^{42,43} while relative energy splittings within the spectra remain unchanged.

Theoretical calculations predict two conduction bands resulting in two possible transitions to the valence band, of which one is parity-allowed and one is parity-forbidden.^{25,29} The notion of parity-allowed and -forbidden transitions only strictly holds for transitions at very specific points in k space, which is not fully applicable to the more extended exciton states in

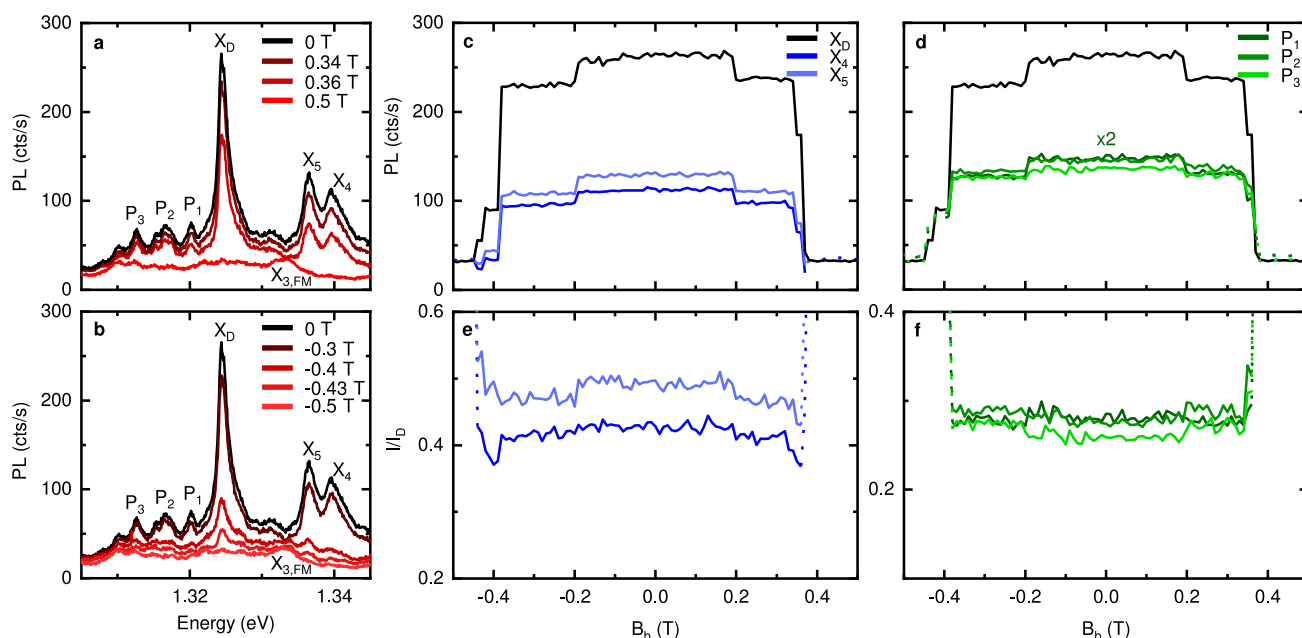


Figure 4. Correlated emissions in magnetic fields. (a) PL emission of the encapsulated CrSBr flake for selected magnetic field strengths B_0 along the crystal b axis and spectral range displaying similar and consistent reduction of the emission intensity with the magnetic field. (b) Same as part a but for negative magnetic fields. (c and d) Maximum intensity of the emissions marked in part a for the magnetic field sweep in Figure S7b. (e and f) Maximum emission intensity in parts c and d normalized by the intensity of X_D . Pointed parts of the graphs indicate regions with large error bars.

CrSBr.⁴⁴ As proposed in other work,^{25,45} we refer to the emission around 1.362 eV (X_B) as the parity-allowed transition. This is in accordance with DR/R measurements displayed in Figure 2c, which reveal an optical resonance with a large oscillator strength at the same energy. This resonance is accompanied by a much weaker resonance roughly 14 meV above this transition (see the transition labeled X^* in Figure 2c). Klein et al.²⁹ suggest that this resonance might have contributions from the same conduction band along the Γ – X direction. In the PL measurements shown, the emission of this transition is absent due to the low excitation power.

For the assignment of the so-called parity-forbidden transition X_D , we refer to work by Lin et al.^{15,45} This corresponds to the brightest transition in the PL emission located around 1.324 eV, 38 meV below X_B , in agreement with previous reports and theoretical predictions for the splitting of exciton energies.^{25,45} We note that the magnitude of the band-gap energy and the origin and magnitude of the splitting between X_B and X_D are discussed in several studies.^{29,32,46–49} Our work adds contrasting magnetic field effects to the observed distinctions between the two transitions. Importantly, we do not observe any signature of X_D in DR/R, in agreement with its parity-forbidden character, i.e., predicted weak oscillator strength.

To gain further insight into the origin of the complex optical response, we performed magnetic field sweeps along the magnetic easy axis (for details, see Methods). For both samples, we observe several abrupt changes in the PL and DR/R at distinctly different magnetic fields. Hence, the magnetization of the sample changes in discrete steps; i.e., different layers in the sample can change their spin orientation individually. We note a certain analogy to layer-by-layer switching in Fe/MgO (001) superlattices,⁵⁰ albeit we use here simple PL and DR/R measurements to monitor the magnetism in CrSBr. Figure 3 displays this layer-by-layer switching in DR/R measurements for the unencapsulated 10-layer sample. In addition to the

resonance of $X_{B,AFM}$, another resonance appears 15 meV red-shifted from it, which we identify as the resonance of X_B in the FM state ($X_{B,FM}$). The resonance of $X_{B,FM}$ appears several 10 mT below the saturation field and persists above it. For this magnetic field range, both resonances $X_{B,AFM}$ and $X_{B,FM}$ are present at the same time; i.e., in these phases, AFM and FM order coexist within the sample. On the basis of our optical mapping experiment, we conclude that the observed resonance superposition does not stem from several domains present within our optical spot size but from layer-specific effects. Figure S5a shows an optical micrograph image of the unencapsulated sample including the 10-layer region. We mapped out a sample region including 10 and 9 layers using DR/R measurements at different magnetic fields shown in Figure S5b,c. The observed magnetic domains are much larger than the measured optical spot size (below 1 μm in diameter). Parts d–f of Figure S5 show that the change of the magnetization state in the magnetic domain relates to the change in the DR/R signal. We observe a discrete transfer of the oscillator strength between $X_{B,AFM}$ and $X_{B,FM}$ with each layer switch shown in Figure 3c. Surprisingly, the measurements reveal an additional resonance red-shifted by 5–7 meV from $X_{B,AFM}$, as shown in Figure 3b. This resonance appears with the first switch of magnetization and remains present until the system fully transitions into the FM state, where it vanishes (see transitions marked by arrows in Figure 3b). The origin of this additional resonance remains to be clarified. We use transfer-matrix analysis (for details, see Methods) to fit the spectra and determine the resonance energies of the oscillators present in the different magnetic phases to be $E_{B,AFM} = 1.366$ eV and $E_{B,FM} = 1.351$ eV. The encapsulated sample exhibits a similar superposition of the individual resonances, as highlighted in Figure S6. In this sample, we determine the respective resonance energies as $E_{B,AFM} = 1.362$ eV and $E_{B,FM} = 1.347$ eV.

In addition to studying transitions with a high oscillator strength in DR/R, we now analyze the magnetic-field-dependent

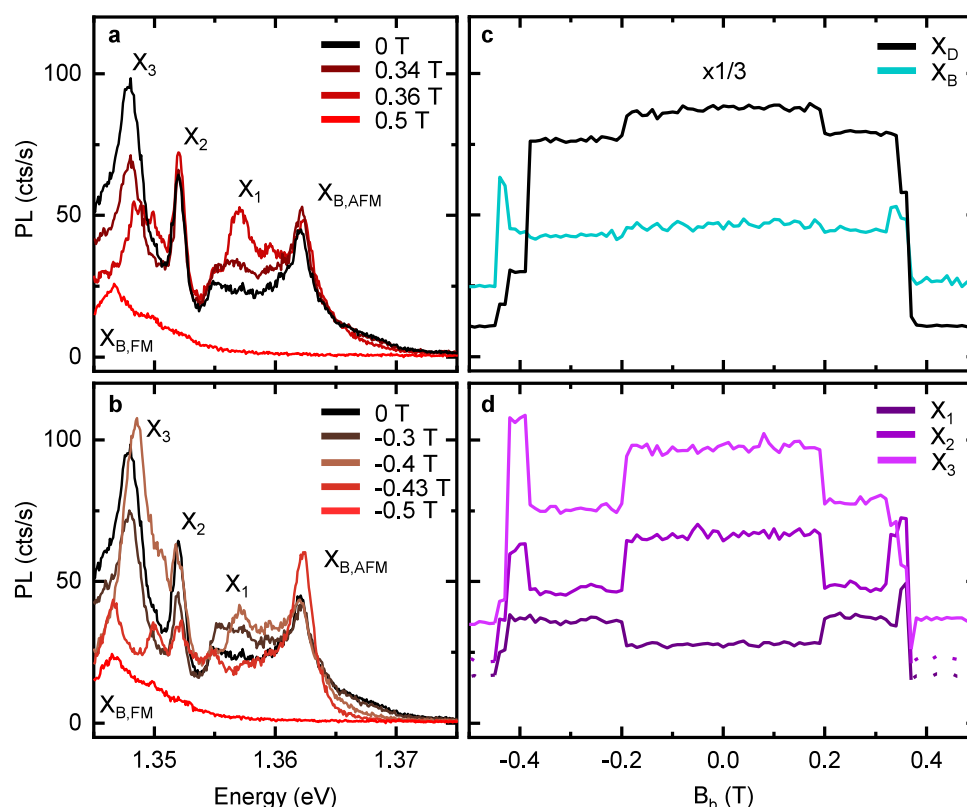


Figure 5. Anticorrelated emissions. (a) PL emission for selected magnetic field strengths and spectral range along the crystal b axis showing unexpected brightening of emissions. (b) Same as part a but for negative magnetic fields. (c) Maximum intensity of the X_B and X_D emissions for the magnetic field sweep in Figure S7b. X_D (X_B) reduces in intensity by $9.5 \pm 2\%$ ($4.1 \pm 4\%$) for $B_b > 0.18$ T and by $12.3 \pm 2\%$ ($8.1 \pm 4.2\%$) for $B_b < -0.2$ T. (d) Maximum intensity of the emissions X_1 , X_2 , and X_3 . Pointed parts of the graphs indicate regions with large error bars.

PL emission, which also gives additional information on exciton species.³⁹ We recorded a full hysteresis loop starting in FM order at negative magnetic field B_b and focus on the down-sweep direction of the measurement loop shown in Figure S7a,b. Parts c and d of Figure S7 display the maximum intensity of X_D and X_B for the whole magnetic field sweep including strong hysteresis effects.

The emission changes most drastically when the magnetic field reaches the saturation field and the remaining layers of the system switch to the FM state. For the down-sweep direction in Figure S7b, this happens at $B_b < -0.44$ T in the encapsulated sample. In the unencapsulated sample, the switch happens at $B_b < -0.37$ T. Due to hysteresis, the FM state starts to vanish at different fields of $B_b < 0.38$ T in the encapsulated sample and $B_b < 0.36$ T in the unencapsulated sample. In the FM state, the emission intensity is much weaker than that in the AFM state, and the emissions experience redshifts of 15 meV for X_B and 12 meV for X_D . This reduction of intensity is thought to result from the reduced layer confinement of excitons in the FM state.⁵¹ In the AFM state, the antiparallel magnetization of adjacent layers does not allow charge transfer between layers, and thus excitons are confined to a layer. However, the parallel magnetization of adjacent layers in the FM state allows charge transfer, reducing the electron–hole wave function overlap. Strikingly, all emission peaks in the investigated samples are weaker in the FM states, while the exact changes during the transition can differ, which we will elaborate on further. In the FM state, the intensities of X_B and X_D reduce by approximately $46 \pm 3\%$ and $88 \pm 1\%$, respectively.

We now turn to a more detailed discussion of the emission changes. Panels a and b of Figure 4 display spectra recorded at different values of B_b in a spectral range around the strongest peak in the PL emission X_D . With increasing magnetic field strength, all of the emission peaks in this range decrease in intensity until either vanishing (within our detection limit) or experiencing an energy shift at the switch to the FM phase. A moderate reduction in intensity appears at $B_b = \pm 0.2$ T, which likely corresponds to a switch of an individual layer magnetization consistent with the observations in Figure 3. Panels c (for transitions X_D , X_4 , and X_5) and d (for transitions P_1 , P_2 , and P_3) of Figure 4 highlight the collective change, where we plot the maximum intensity of each of the emissions. We emphasize this further by plotting the intensity ratios of the emissions compared to the emission of X_D in Figure 4e,f. Until fully switching to the FM phase, the intensity ratios stay almost constant. We want to emphasize that, in addition, before reaching B_b^s , none of these emissions exhibit an energy shift despite the changes in intensity. This correlated behavior suggests that these emissions stem from the same band transition.

The emissions P_1 , P_2 , and P_3 are red-shifted with respect to X_D by 4.2, 7.8, and 11.9 meV, respectively, i.e., approximately equidistantly spaced by 4 meV. From this, one might speculate that the emissions P_1 , P_2 , and P_3 are phonon replicas of X_D . However, the intensity changes of the PL emission of P_1 with excitation power and temperature suggest trapped exciton character, as described before. Within the resolution of the observed PL spectra, we cannot identify the presence of P_{1-3} in the FM phase. We note that, in the energy range of the P_{1-3} , phonon replicas of X_D with the A_g^1 mode have been reported.¹⁵

At higher excitation powers, we find signatures of these emissions overlaid with P_{1-3} . The attribution of X_4 and X_5 , centered around 1.339 and 1.336 eV, respectively, needs to be clarified in further studies. At this point, we can report that X_4 and X_5 show an evolution with magnetic field B_b that is similar to that of X_D . However, in FM order, the emission peaks of X_4 and X_5 are not discernible anymore.

While the emission peaks between 1.31 and 1.345 eV experience very similar emission changes in magnetic fields compared to X_D , the emissions X_B and X_{1-3} between 1.345 and 1.37 eV behave very differently. Panels a and b of Figure 5 show spectra in this energy range for the same magnetic field values as those in Figure 4a,b. At zero magnetic field, the emission energies of X_{1-3} are located at $E_1 = 1.355$ eV, $E_2 = 1.352$ eV, and $E_3 = 1.348$ eV. Most strikingly, the intensity of X_B as a function of B_b evolves very differently compared to that of X_D , as highlighted in Figure 5c and compared to Figure S7c,d. As described before, the intensity of X_D decreases measurably as individual layers flip the spin orientation. In contrast, the intensity of X_B reduces less, as highlighted in Figure 5c. Very surprisingly, at magnetic fields close to the transition to the FM state, the intensity of X_B increases. Similar to X_B , also the transitions X_1 , X_2 , and X_3 experience an increase in intensity close to the saturation field. Additionally, X_2 and X_3 initially decrease in intensity with the single-layer switch at $B_b = \pm 0.2$ T. In contrast, at $B_b = \pm 0.2$ T, the transition X_1 increases its intensity. Despite the changes, X_B and X_2 do not shift in energy before the transition to the FM state. However, X_1 and X_3 experience a slight blueshift, as shown in Figure 5a,b.

Above B_b^* , the entire crystal is in the FM state. As described above, for applied magnetic fields $0 < B_{\text{applied}} < B_b^*$, AFM and FM order can coexist in the crystal (Figure 3a). Similar to the DR/R measurements, we observe spectral features of both orders in the PL measurements. For example, the emission peak of, e.g., $X_{3,\text{FM}}$ is overlaid with the weakened emission peaks of X_4 and X_5 of AFM order, as highlighted in Figure 4b. Similarly, the emission peak of $X_{B,\text{FM}}$ is overlaid with the emission peak of X_3 displayed in Figure 5a,b. For the other emission peaks, this superposition is less visible although present.

III. CONCLUSION

In conclusion, photoluminescence and differential reflectance contrast DR/R measurements reveal steplike changes in intensity for all observed emission peaks correlated to a layer-by-layer switching of the magnetization for fields applied along the magnetic easy axis. Some of these emissions around the parity-forbidden transition X_D reduce monotonously with increasing magnetic field and do not experience energy shifts until the saturation field along B_b . We find several exceptions from this trend between X_D and X_B , which do experience energy shifts and even increase in intensity close to the saturation field. Excitation-power-dependent and temperature-dependent PL measurements indicate the presence of trapped exciton species. Of the multitude of emission peaks, only X_B , X_3 , and X_D remain present up to $T = 100$ K. Additionally, we find that, in phases close to the transition to the FM state, excitonic emission and absorption from AFM and FM order coexist.

IV. METHODS

A. Sample Fabrication. Bulk CrSBr crystals were fabricated through chemical vapor transport.⁵² Nanometer-thin CrSBr and hBN flakes were mechanically exfoliated onto poly(dimethylsiloxane) and transferred onto Si substrates with an 80-nm-thick oxide layer. The

layer thicknesses were determined using an atomic force microscope (Oxford Instruments Cypher) equipped with AC160 cantilevers (Oxford Instruments). Atomic force microscopy yields a CrSBr thickness of 8.2 ± 0.3 nm (11.3 ± 0.2 nm) corresponding to 10 (14) layers for the unencapsulated (encapsulated) sample. Both samples were annealed at 200 degrees for several hours.

B. Optical Spectroscopy. Optical spectroscopy was carried out in a home-built confocal setup for magneto-optical spectroscopy.³⁹ The sample was placed inside a closed-cycle cryostat (attocube systems, AttoDry 1000XL) equipped with a vector magnet (z axis, solenoid, maximum field = 5 T; x/y axis, split coil, maximum field = 2 T). We used low-temperature piezopositioners (attocube systems, ANPx101 and ANPz102) to position the sample with respect to a low-temperature apochromatic objective. PL and DR/R measurements were performed in backscattering geometry at a sample temperature of 4.7 K. The signal was dispersed inside a Czerny–Turner spectrograph (Teledyne Princeton Instruments, SpectraPro HRS-500) and detected by a CCD camera (Teledyne Princeton Instruments, Pylon BRExcelon 100). For DR/R measurements, we used a tungsten–halogen lamp (Thorlabs, SLS201L/M) polarized along the crystal b axis by a nanoparticle–film polarizer and an achromatic half-waveplate. For PL measurements, we used a HeNe laser (Thorlabs, HNL210LB) with its polarization aligned along the crystal a axis, while the emission was detected along the b axis. PL measurements were performed at excitation powers ranging from 0.2 to 260 μW . Magnetic-field-dependent measurements were performed by initializing the CrSBr sample in the FM state, ramping the magnet to -0.6 T (-0.5 T) for the encapsulated 14-layer (unencapsulated, 10-layer) sample, followed by a sweep to 0.6 T (0.5 T) and subsequent inversion of the sweep direction to obtain a full hysteresis.

C. Transfer-Matrix Analysis. For analysis of the DR/R measurements, we apply a transfer-matrix formalism,^{18,19,53} using a Lorentzian oscillator model for the dielectric constant of CrSBr:

$$\epsilon(\omega) = \epsilon_\infty + \sum_j \frac{f_j/\hbar^2}{\omega_j^2 - \omega^2 - i\Gamma_j\omega} \quad (1)$$

where ω_j and Γ_j denote the oscillator frequency and decay rate and f_j denotes the oscillator strength of the j th oscillator. We account for a constant background permittivity $\epsilon_\infty = 10$, similar to Wang et al.,¹⁹ and use the permittivities $\epsilon_{\text{SiO}_2} = 2.1$,⁵⁴ $\epsilon_{\text{Si}} = 13$ ⁵⁵ and $\epsilon_{\text{hBN}} = 4.6$.⁵⁶

ASSOCIATED CONTENT

Supporting Information

The Supporting Information is available free of charge at <https://pubs.acs.org/doi/10.1021/acsnano.5c05470>.

Polarization-dependent PL measurements of the encapsulated sample, comparative PL spectra of the two samples and excitation-power-dependent PL of the unencapsulated sample, comparison of the DR/R and PL spectra in the AFM and FM order, excitation-power-dependent PL intensities, temperature-dependent PL measurements, sample image and domain mapping using DR/R measurements, transfer-matrix analysis for the DR/R spectra recorded at selected magnetic field strengths, and PL hysteresis and measurement of the PL emission intensities of X_B and X_D for the full hysteresis of the encapsulated and unencapsulated samples (PDF)

AUTHOR INFORMATION

Corresponding Author

Bernhard Urbaszek – Institute for Condensed Matter Physics, TU Darmstadt, D-64289 Darmstadt, Germany; orcid.org/0000-0003-0226-7983; Email: bernhard.urbaszek@pkm.tu-darmstadt.de

Authors

Lukas Krelle – Institute for Condensed Matter Physics, TU Darmstadt, D-64289 Darmstadt, Germany; orcid.org/0009-0005-2981-6112

Ryan Tan – Institute for Condensed Matter Physics, TU Darmstadt, D-64289 Darmstadt, Germany

Daria Markina – Institute for Condensed Matter Physics, TU Darmstadt, D-64289 Darmstadt, Germany

Priyanka Mondal – Institute for Condensed Matter Physics, TU Darmstadt, D-64289 Darmstadt, Germany

Kseniia Mosina – Department of Inorganic Chemistry, University of Chemistry and Technology Prague, 16628 Prague 6, Czech Republic; orcid.org/0000-0003-3570-5337

Kevin Hagmann – Institute for Condensed Matter Physics, TU Darmstadt, D-64289 Darmstadt, Germany

Regine von Klitzing – Institute for Condensed Matter Physics, TU Darmstadt, D-64289 Darmstadt, Germany

Kenji Watanabe – Research Center for Electronic and Optical Materials, National Institute for Materials Science, Tsukuba 305-0044, Japan; orcid.org/0000-0003-3701-8119

Takashi Taniguchi – Research Center for Materials Nanoarchitectonics, National Institute for Materials Science, Tsukuba 305-0044, Japan; orcid.org/0000-0002-1467-3105

Zdenek Sofer – Department of Inorganic Chemistry, University of Chemistry and Technology Prague, 16628 Prague 6, Czech Republic

Complete contact information is available at:

<https://pubs.acs.org/10.1021/acsnano.5c05470>

Author Contributions

K.M. and Z.S. grew bulk CrSBr crystals. T.T. and K.W. grew bulk hBN crystals. L.K. fabricated the samples and performed optical spectroscopy with R.T.. P.M., L.K., K.H., and R.v.K. performed and analyzed the AFM measurements. L.K., R.T., and B.U. analyzed the optical spectra. L.K., R.T., P.M., D.M., and B.U. discussed the results. B.U. suggested the experiments and supervised the project. L.K., R.T., and B.U. wrote the manuscript. All authors contributed to the final manuscript.

Notes

The authors declare no competing financial interest.

ACKNOWLEDGMENTS

We thank Florian Dirnberger for fruitful discussions. K.W. and T.T. acknowledge support from the JSPS KAKENHI (Grants 21H05233 and 23H02052), CREST (JPMJCR24A5), JST, and World Premier International Research Center Initiative, MEXT, Japan. Z.S. was supported by the ERC-CZ program (Project LL2101) from the Ministry of Education Youth and Sports and by the project Advanced Functional Nanorobots (Reg. No. CZ.02.1.01/0.0/0.0/15-003/0000444 financed by the EFRR).

REFERENCES

- (1) Gibertini, M.; Koperski, M.; Morpurgo, A. F.; Novoselov, K. S. Magnetic 2D materials and heterostructures. *Nat. Nanotechnol.* **2019**, *14*, 408.
- (2) Song, T.; Cai, X.; Tu, M. W.-Y.; Zhang, X.; Huang, B.; Wilson, N. P.; Seyler, K. L.; Zhu, L.; Taniguchi, T.; Watanabe, K.; et al. Giant tunneling magnetoresistance in spin-filter van der waals heterostructures. *Science* **2018**, *360*, 1214.
- (3) Wang, Z.; Gutiérrez-Lezama, I.; Ubrig, N.; Kroner, M.; Gibertini, M.; Taniguchi, T.; Watanabe, K.; Imamoğlu, A.; Giannini, E.; Morpurgo, A. F. Very large tunneling magnetoresistance in layered magnetic semiconductor CrI₃. *Nat. Commun.* **2018**, *9*, 2516.
- (4) Ahn, E. C. 2D materials for spintronic devices. *npj 2D Mater. Appl.* **2020**, *4*, 17.
- (5) Mi, M.; Xiao, H.; Yu, L.; Zhang, Y.; Wang, Y.; Cao, Q.; Wang, Y. Two-dimensional magnetic materials for spintronic devices. *Mater. Today Nano* **2023**, *24*, 100408.
- (6) Liu, Y.; Wang, W.; Lu, H.; Xie, Q.; Chen, L.; Yin, H.; Cheng, G.; Wu, X. The environmental stability characterization of exfoliated few-layer CrXTe₃ (X = Si, Ge) nanosheets. *Appl. Surf. Sci.* **2020**, *511*, 145452.
- (7) Galbiati, M.; Zatko, V.; Godel, F.; Hirschauer, P.; Vecchiola, A.; Bouzehouane, K.; Collin, S.; Servet, B.; Cantarero, A.; Petroff, F.; et al. Very long term stabilization of a 2D magnet down to the monolayer for device integration. *ACS Appl. Electron. Mater.* **2020**, *2*, 3508.
- (8) Gish, J. T.; Lebedev, D.; Stanev, T. K.; Jiang, S.; Georgopoulos, L.; Song, T. W.; Lim, G.; Garvey, E. S.; Valdman, L.; Balogun, O.; et al. Ambient-stable two-dimensional CrI₃ via organic-inorganic encapsulation. *ACS Nano* **2021**, *15*, 10659.
- (9) Shcherbakov, D.; Stepanov, P.; Weber, D.; Wang, Y.; Hu, J.; Zhu, Y.; Watanabe, K.; Taniguchi, T.; Mao, Z.; Windl, W.; et al. Raman spectroscopy, photocatalytic degradation, and stabilization of atomically thin chromium tri-iodide. *Nano Lett.* **2018**, *18*, 4214.
- (10) Ziebel, M. E.; Feuer, M. L.; Cox, J.; Zhu, X.; Dean, C. R.; Roy, X. Crsbr: an air-stable, two-dimensional magnetic semiconductor. *Nano Lett.* **2024**, *24*, 4319.
- (11) Ye, C.; Wang, C.; Wu, Q.; Liu, S.; Zhou, J.; Wang, G.; Soll, A.; Sofer, Z.; Yue, M.; Liu, X.; et al. Layer-dependent interlayer antiferromagnetic spin reorientation in air-stable semiconductor CrSBr. *ACS Nano* **2022**, *16*, 11876.
- (12) Bae, Y. J.; Wang, J.; Scheie, A.; Xu, J.; Chica, D. G.; Diederich, G. M.; Cenker, J.; Ziebel, M. E.; Bai, Y.; Ren, H.; et al. Exciton-coupled coherent magnons in a 2D semiconductor. *Nature* **2022**, *609*, 282.
- (13) Diederich, G. M.; Cenker, J.; Ren, Y.; Fonseca, J.; Chica, D. G.; Bae, Y. J.; Zhu, X.; Roy, X.; Cao, T.; Xiao, D.; et al. Tunable interaction between excitons and hybridized magnons in a layered semiconductor. *Nat. Nanotechnol.* **2023**, *18*, 23.
- (14) Diederich, G. M.; Nguyen, M.; Cenker, J.; Fonseca, J.; Pumulo, S.; Bae, Y. J.; Chica, D. G.; Roy, X.; Zhu, X.; Xiao, D.; Ren, Y.; Xu, X. Exciton dressing by extreme nonlinear magnons in a layered semiconductor. *Nat. Nanotechnol.* **2025**, *20*, 617.
- (15) Lin, K.; Sun, X.; Dirnberger, F.; Li, Y.; Qu, J.; Wen, P.; Sofer, Z.; Söll, A.; Winnerl, S.; Helm, M.; et al. Strong exciton–phonon coupling as a fingerprint of magnetic ordering in van der waals layered CrSBr. *ACS Nano* **2024**, *18*, 2898.
- (16) Mondal, P.; Markina, D. I.; Hopf, L.; Krelle, L.; Shradha, S.; Klein, J.; Glazov, M. M.; Gerber, I.; Hagmann, K.; Klitzing, R. v.; et al. Raman polarization switching in CrSBr. *npj 2D Mater. Appl.* **2025**, *9*, 22.
- (17) Sahu, S.; Berrezueta-Palacios, C.; Juergensen, S.; Mosina, K.; Sofer, Z.; Velický, M.; Kusch, P.; Frank, O. Resonance raman scattering and anomalous anti-stokes phenomena in CrSBr. *Nanoscale* **2025**, *17*, 11539.
- (18) Dirnberger, F.; Quan, J.; Bushati, R.; Diederich, G. M.; Florian, M.; Klein, J.; Mosina, K.; Sofer, Z.; Xu, X.; Kamra, A.; et al. Magneto-optics in a van der waals magnet tuned by self-hybridized polaritons. *Nature* **2023**, *620*, 533.
- (19) Wang, T.; Zhang, D.; Yang, S.; Lin, Z.; Chen, Q.; Yang, J.; Gong, Q.; Chen, Z.; Ye, Y.; Liu, W. Magnetically-dressed CrSBr exciton-polaritons in ultrastrong coupling regime. *Nat. Commun.* **2023**, *14*, 5966.
- (20) Li, C.; Shen, C.; Jiang, N.; Tang, K. K.; Liu, X.; Guo, J.; Liang, Y.; Song, J.; Deng, X.; Zhang, Q. 2d crsbr enables magnetically controllable exciton-polaritons in an open cavity. *Adv. Funct. Mater.* **2024**, *34*, 2411589.
- (21) Nessi, L.; Occhialini, C. A.; Demir, A. K.; Powalla, L.; Comin, R. Magnetic field tunable polaritons in the ultrastrong coupling regime in CrSBr. *ACS Nano* **2024**, *18*, 34235.
- (22) Han, B.; Shan, H.; Song, K. W.; Lackner, L.; Esmann, M.; Solovyeva, V.; Eilenberger, F.; Regner, J.; Sofer, Z.; Kyriienko, O.; et al.

Exciton-polariton condensate in the van der waals magnet CrSBr. *arXiv* **2025**, DOI: 10.48550/arXiv.2501.18233.

(23) Boix-Constant, C.; Mañas-Valero, S.; Ruiz, A. M.; Rybakov, A.; Konieczny, K. A.; Pillet, S.; Baldoví, J. J.; Coronado, E. Probing the spin dimensionality in single-layer CrSBr van der waals heterostructures by magneto-transport measurements. *Adv. Mater.* **2022**, *34*, 2204940.

(24) Telford, E. J.; Dismukes, A. H.; Lee, K.; Cheng, M.; Wieteska, A.; Bartholomew, A. K.; Chen, Y.-S.; Xu, X.; Pasupathy, A. N.; Zhu, X.; Dean, C. R.; Roy, X. Layered antiferromagnetism induces large negative magnetoresistance in the van der waals semiconductor CrSBr. *Adv. Mater.* **2020**, *32*, 2003240.

(25) Wilson, N. P.; Lee, K.; Cenker, J.; Xie, K.; Dismukes, A. H.; Telford, E. J.; Fonseca, J.; Sivakumar, S.; Dean, C.; Cao, T.; et al. Interlayer electronic coupling on demand in a 2D magnetic semiconductor. *Nat. Mater.* **2021**, *20*, 1657.

(26) Tabataba-Vakili, F.; Nguyen, H. P. G.; Rupp, A.; Mosina, K.; Papavasileiou, A.; Watanabe, K.; Taniguchi, T.; Maletinsky, P.; Glazov, M. M.; Sofer, Z.; Baimuratov, A. S.; Hoge, A. Doping-control of excitons and magnetism in few-layer CrSBr. *Nat. Commun.* **2024**, *15*, 4735.

(27) Long, F.; Ghorbani-Asl, M.; Mosina, K.; Li, Y.; Lin, K.; Ganss, F.; Hübner, R.; Sofer, Z.; Dirnberger, F.; Kamra, A.; et al. Ferromagnetic interlayer coupling in CrSBr crystals irradiated by ions. *Nano Lett.* **2023**, *23*, 8468.

(28) Long, F.; Li, Y.; Cheng, Y.; Mosina, K.; Kentsch, U.; Sofer, Z.; Prucnal, S.; Helm, M.; Zhou, S. Rise and fall of the ferromagnetism in CrSBr flakes by non-magnetic ion irradiation. *Adv. Phys. Res.* **2024**, *3*, 2400053.

(29) Klein, J.; Pingault, B.; Florian, M.; Heißenbüttel, M.-C.; Steinhoff, A.; Song, Z.; Torres, K.; Dirnberger, F.; Curtis, J. B.; Weile, M.; et al. The bulk van der waals layered magnet CrSBr is a quasi-1D material. *ACS Nano* **2023**, *17*, 5316.

(30) Yang, K.; Wang, G.; Liu, L.; Lu, D.; Wu, H. Triaxial magnetic anisotropy in the two-dimensional ferromagnetic semiconductor CrSBr. *Phys. Rev. B* **2021**, *104*, 144416.

(31) Liebich, M.; Florian, M.; Nilforoushan, N.; Mooshammer, F.; Koulouklidis, A. D.; Wittmann, L.; Mosina, K.; Sofer, Z.; Dirnberger, F.; Kira, M.; Huber, R. Controlling coulomb correlations and fine structure of quasi-one-dimensional excitons by magnetic order. *Nat. Mater.* **2025**, *24*, 384.

(32) Shao, Y.; Dirnberger, F.; Qiu, S.; Acharya, S.; Terres, S.; Telford, E. J.; Pashov, D.; Kim, B. S.; Ruta, F. L.; Chica, D. G. Magnetically confined surface and bulk excitons in a layered antiferromagnet. *Nat. Mater.* **2025**, *24*, 391.

(33) Tschudin, M. A.; Broadway, D. A.; Siegwolf, P.; Schrader, C.; Telford, E. J.; Gross, B.; Cox, J.; Dubois, A. E.; Chica, D. G.; Rama-Eiroa, R.; et al. Imaging nanomagnetism and magnetic phase transitions in atomically thin CrSBr. *Nat. Commun.* **2024**, *15*, 6005.

(34) Rizzo, D. J.; McLeod, A. S.; Carnahan, C.; Telford, E. J.; Dismukes, A. H.; Wiscons, R. A.; Dong, Y.; Nuckolls, C.; Dean, C. R.; Pasupathy, A. N.; et al. Visualizing atomically layered magnetism in CrSBr. *Adv. Mater.* **2022**, *34*, 2201000.

(35) Lee, K.; Dismukes, A. H.; Telford, E. J.; Wiscons, R. A.; Wang, J.; Xu, X.; Nuckolls, C.; Dean, C. R.; Roy, X.; Zhu, X. Magnetic order and symmetry in the 2d semiconductor CrSBr. *Nano Lett.* **2021**, *21*, 3511.

(36) Göser, O.; Paul, W.; Kahle, H. Magnetic properties of CrSBr. *J. Magn. Magn. Mater.* **1990**, *92*, 129.

(37) Wang, G.; Robert, C.; Glazov, M. M.; Cadiz, F.; Courtade, E.; Amand, T.; Lagarde, D.; Taniguchi, T.; Watanabe, K.; Urbaszek, B.; et al. In-plane propagation of light in transition metal dichalcogenide monolayers: optical selection rules. *Phys. Rev. Lett.* **2017**, *119*, 047401.

(38) He, M.; Rivera, P.; Van Tuan, D.; Wilson, N. P.; Yang, M.; Taniguchi, T.; Watanabe, K.; Yan, J.; Mandrus, D. G.; Yu, H.; et al. Valley phonons and exciton complexes in a monolayer semiconductor. *Nat. Commun.* **2020**, *11*, 618.

(39) Shree, S.; Paradisanos, I.; Marie, X.; Robert, C.; Urbaszek, B. Guide to optical spectroscopy of layered semiconductors. *Nat. Rev. Phys.* **2021**, *3*, 39.

(40) Godde, T.; Schmidt, D.; Schmutzler, J.; Aßmann, M.; Debus, J.; Withers, F.; Alexeev, E.; Del Pozo-Zamudio, O.; Skrypkina, O.; Novoselov, K.; et al. Exciton and trion dynamics in atomically thin MoSe₂ and WSe₂: Effect of localization. *Phys. Rev. B* **2016**, *94*, 165301.

(41) Huang, X.; Song, Z.; Gao, Y.; Gu, P.; Watanabe, K.; Taniguchi, T.; Yang, S.; Chen, Z.; Ye, Y. Intrinsic localized excitons in MoSe₂/CrSBr heterostructure. *Adv. Mater.* **2025**, *37*, 2413438.

(42) Raja, A.; Chaves, A.; Yu, J.; Arefe, G.; Hill, H. M.; Rigosi, A. F.; Berkelbach, T. C.; Nagler, P.; Schüller, C.; Korn, T.; et al. Coulomb engineering of the bandgap and excitons in two-dimensional materials. *Nat. Commun.* **2017**, *8*, 15251.

(43) Stier, A. V.; Wilson, N. P.; Clark, G.; Xu, X.; Crooker, S. A. Probing the influence of dielectric environment on excitons in monolayer WSe₂: insight from high magnetic fields. *Nano Lett.* **2016**, *16*, 7054.

(44) Bianchi, M.; Acharya, S.; Dirnberger, F.; Klein, J.; Pashov, D.; Mosina, K.; Sofer, Z.; Rudenko, A. N.; Katsnelson, M. I.; Van Schilfgaarde, M.; et al. Paramagnetic electronic structure of crsbr: Comparison between ab initio gw theory and angle-resolved photoemission spectroscopy. *Phys. Rev. B* **2023**, *107*, 235107.

(45) Lin, K.; Li, Y.; Ghorbani-Asl, M.; Sofer, Z.; Winnerl, S.; Erbe, A.; Krashenninnikov, A. V.; Helm, M.; Zhou, S.; Dan, Y.; et al. Probing the band splitting near the γ point in the van der waals magnetic semiconductor CrSBr. *J. Phys. Chem. Lett.* **2024**, *15*, 6010.

(46) Komar, R.; Lopion, A.; Goryca, M.; Rybak, M.; Woźniak, T.; Mosina, K.; Söll, A.; Sofer, Z.; Pacuski, W.; Faugeras, C.; et al. Colossal magneto-excitonic effects in 2D van der waals magnetic semiconductor crsbr. *arXiv* **2024**, DOI: 10.48550/arXiv.2409.00187.

(47) Smolenski, S.; Wen, M.; Li, Q.; Downey, E.; Alfrey, A.; Liu, W.; Kondusamy, A. L.; Bostwick, A.; Jozwiak, C.; Rotenberg, E.; et al. Large exciton binding energy in a bulk van der waals magnet from quasi-1D electronic localization. *Nat. Commun.* **2025**, *16*, 1134.

(48) Qian, T.-X.; Zhou, J.; Cai, T.-Y.; Ju, S. Anisotropic electron-hole excitation and large linear dichroism in the two-dimensional ferromagnet CrSBr with in-plane magnetization. *Phys. Rev. Res.* **2023**, *5*, 033143.

(49) Datta, B.; Adak, P. C.; Yu, S.; Valiyaparambil Dharmapalan, A.; Hall, S. J.; Vakulenko, A.; Komissarenko, F.; Kurganov, E.; Quan, J.; Wang, W. Magnon-mediated exciton-exciton interaction in a van der waals antiferromagnet. *Nat. Mater.* **2025**, *1*, 1027.

(50) Moubah, R.; Magnus, F.; Warnatz, T.; Pálsson, G. K.; Kapaklis, V.; Ukleev, V.; Devishvili, A.; Palisaitis, J.; Persson, P.; Hjörvarsson, B. Discrete layer-by-layer magnetic switching in Fe/MgO (001) superlattices. *Phys. Rev. Appl.* **2016**, *5*, 044011.

(51) Marques-Moros, F.; Boix-Constant, C.; Mañas-Valero, S.; Canet-Ferrer, J.; Coronado, E. Interplay between optical emission and magnetism in the van der waals magnetic semiconductor CrSBr in the two-dimensional limit. *ACS Nano* **2023**, *17*, 13224.

(52) Klein, J.; Pham, T.; Thomsen, J.; Curtis, J.; Denneulin, T.; Lorke, M.; Florian, M.; Steinhoff, A.; Wiscons, R.; Luxa, J.; et al. Control of structure and spin texture in the van der waals layered magnet CrSBr. *Nat. Commun.* **2022**, *13*, 5420.

(53) Robert, C.; Semina, M.; Cadiz, F.; Manca, M.; Courtade, E.; Taniguchi, T.; Watanabe, K.; Cai, H.; Tongay, S.; Lassagne, B.; et al. Optical spectroscopy of excited exciton states in MoS₂ monolayers in van der waals heterostructures. *Phys. Rev. Mater.* **2018**, *2*, 011001.

(54) Malitson, I. H. Interspecimen comparison of the refractive index of fused silica. *J. Opt. Soc. Am.* **1965**, *55*, 1205.

(55) Schinke, C.; Christian Peest, P.; Schmidt, J.; Brendel, R.; Bothe, K.; Vogt, M. R.; Winter, S.; Schirmacher, A.; Lim, S.; Nguyen, H. T.; MacDonald, D. Uncertainty analysis for the coefficient of band-to-band absorption of crystalline silicon. *AIP Adv.* **2015**, *5*, DOI: 10.1063/1.4923379.

(56) Lee, S.-Y.; Jeong, T.-Y.; Jung, S.; Yee, K.-J. Refractive index dispersion of hexagonal boron nitride in the visible and near-infrared. *Phys. Status Solidi B* **2019**, *256*, 1800417.